Available online at www.sciencedirect.com
SCIENCE DIRECT®
Journal of Solid State Chemistry 177 (2004) 89–100
JOURNAL OF SOLID STATE CHEMISTRY
http://elsevier.com/locate/jssc

Optical properties of $CeBO_3$ and CeB_3O_6 compounds: first-principles calculations and experimental results

F. Goubin,[a] Y. Montardi,[b] P. Deniard,[a] X. Rocquefelte,[a] R. Brec,[a] and S. Jobic[a,*]

[a] *Institut des Matériaux Jean Rouxel, UMR 6502 Université de Nantes–CNRS, Laboratoire de Chimie des Solides, 2 rue de la Houssinière, BP 32229, 44322 Nantes Cedex 03, France*

[b] *Rhodia Electronics & Catalysis, 52 rue de la Haie Coq, Aubervilliers, 93308, France*

Received 14 January 2003; received in revised form 22 May 2003; accepted 30 May 2003

Abstract

The cerium borates *o*-$CeBO_3$, *m*-$CeBO_3$ and CeB_3O_6 have been shown to be isostructural to their lanthanum derivatives. From diffuse reflectance, electron energy loss spectroscopy (EELS) and band structure calculations, it has been evidenced that a Ce^{3+} $4f-5d$ transition is responsible for weak absorption peaks around 3.5 eV while the $O2p-Ce5d$ charge transfer gives rise to a strong absorption around 7 eV. Starting from self-consistent full potential LAPW calculations, the dielectric tensors of the three compounds were computed and compared to experimental data. It results in a satisfactory fit between the observed and the calculated extinction coefficient k and the index of refraction n.

Keywords: Cerium borates; UV absorbers; Optical properties; Diffuse reflectance; EELS; Dielectric function

1. Introduction

Europium and/or terbium-doped rare-earth orthoborates MBO_3 (M = Sc, Y, La, Gd, Lu) have experienced a remarkable development during the last decade due to their interesting luminescence properties [1,2]. Current investigations often focus more, particularly, on the applications of these materials as phosphors in fluorescent lighting and plasma display panel (PDP) [3], where luminescent materials are needed to convert high-energy radiation into visible light. To this end, the $(Y,Gd)BO_3:Eu^{3+}$ materials are widely used as phosphors [4]: with a valence band–conduction band gap above 6 eV, these Eu^{3+} activated compounds exhibit an excellent quantum efficiency owing to the perfect fitting between their energy gap and the maximum emission intensity of the Ne–Xe plasma. Potential interest of cerium borates could be an application as UV shields. As f levels are inter-spaced between the valence band (vb) and the conduction band (cb), the absorption threshold might lie in effect around 3 eV. In this context, we have embarked on the investigation of the optical properties of Ce-containing borates as possible UV absorbers.

The importance of these studies originates in the fact that in recent years, the consumer market has requested high protection in both UV-B (290–320 nm) and UV-A (320–400 nm) regions. Since the first organic UV absorbers show effective UV-B absorption properties but modest UV-A absorbing capability [5], cosmetic preparation containing nano-particle titanium and zinc oxides appeared as ideal substitutes due to a steep absorption onset at 3.1 and 3.2 eV for TiO_2 and ZnO, respectively, giving a wide absorption range (UV-A and -B) with health compatibility. These properties explain their intensive use by the cosmetic industry today. Unfortunately, these interesting absorption characteristics go along with drawbacks, such as a significant photocatalytic activity for TiO_2 and a high refractive index (2.8 and 2.1 at 530 nm for titanium and zinc oxides, respectively). The former may induce a deterioration of the medium [6] in which the mineral is embedded for application (oxidation and degradation of the organic matrix for instance) while the latter induces a whitish aspect. For these reasons, there is a strong motivation to develop new (second generation) UV absorbers. Recall that the major difference between

*Corresponding author. Fax: 33-2-40-37-39-95.
E-mail address: jobic@cnrs-imn.fr (S. Jobic).

0022-4596/03/$ - see front matter © 2003 Elsevier Inc. All rights reserved.
doi:10.1016/S0022-4596(03)00322-0

pigments and UV absorbers do not lie only in the position of the absorption threshold but also in the value of the refractive index. Hence, light scattering in the visible region has to be minimized in UV absorbers (low n index), while the opposite is requested for pigment (high n index). Thus, based on this requirement, TiO_2 and ZnO have rather to be considered as white pigments (their UV shielding properties being a combination of absorption and scattering), while Ce-containing borates, provided they present the requested ~ 3 eV absorption threshold, appear as appropriate materials as UV absorbers (their refractive index being expected to be lower than 2 [7]).

Due to the lack of data on the absorption threshold of Ce-containing borates, the synthesis of the two allotropic varieties of $CeBO_3$ and CeB_3O_6 has been carried out by conventional solid state reactions. After structural characterization, optical properties have been determined from diffuse reflectance measurement and electron energy loss spectroscopy (EELS). Ab initio calculation has been carried out to correlate the crystal structures and properties and to get some insights concerning the variation of the optical constant with the energy of the incident beam.

2. Experimental

2.1. Synthesis

The two allotropic forms of $CeBO_3$ (m-$CeBO_3$, monoclinic, and o-$CeBO_3$, orthorhombic) and CeB_3O_6 were prepared by the ceramic method from a mixture of hydrated cerium nitrate ($Ce(NO_3)_3$, $6H_2O$, Prolabo, 99.5%) and boric acid (H_3BO_3, Prolabo, 98%) heated under hydrogen (Air Liquide, 99%, ~ 2 L/h) flux in an alumina boat. 200°C/h heating and cooling rate were applied for all the samples. Syntheses in air systematically led to the formation of a large amount of CeO_2.

(a) *o-CeBO₃*: 2.170 g (5 mmol) of $Ce(NO_3)_3$, $6H_2O$ and 0.334 g (5.4 mmol) H_3BO_3 (B/Ce ratio of 1.08) were heated at 900°C for 24 h. A homogeneous white powder was then obtained which turned out to contain also a small amount of m-$CeBO_3$. From a Rietveld analysis of the X-ray pattern, the impurity weight percentage was calculated at 2.3(2)%. Attempts to prepare pure o-$CeBO_3$ were unsuccessful. The use of hydrogen flow (to prevent the oxidation of Ce^{3+} into Ce^{4+}) made it impossible to carry out quenching of the sample in air.

(b) *m-CeBO₃*: 2.170 g (5 mmol) $Ce(NO_3)_3$, $6H_2O$ and 0.321 g (5.2 mmol) H_3BO_3 (B/Ce ratio of 1.04) were heated at 600°C for 1 day. Unfortunately, it contained white and brown grains. Changes in the ratio of the pristine materials, reaction temperature plateau and/or synthesis duration, did not improve the color homogeneity of the samples. A microprobe analysis by energy dispersive X-ray spectroscopy (EDXS) did not reveal chemical elements other than Ce and an XRD analysis evidenced neither an amorphous phase, nor a crystallized impurity, but only the presence of m-$CeBO_3$. From chemical criteria, the occurrence of grains of different colors remains unexplained.

(c) *CeB₃O₆*: 1.086 g (2.5 mmol) $Ce(NO_3)_3$, $6H_2O$ and 1.854 g (30 mmol) H_3BO_3 (B/Ce ratio of 12) were heated at 800°C for 1 h. The white powder obtained was then washed with distilled water to remove the excess of boric acid and to obtain pure CeB_3O_6.

2.2. X-ray structure determination

The X-ray powder diffraction patterns were collected from a Siemens D5000 diffractometer without monochromator (CuK-$L_{3,2}$, $\lambda = 1.540598$ and 1.544390 Å; reflection geometry; linear detector with a 0.18°/min sweep speed; 2θ range = 10–120° for o- and m-$CeBO_3$, 13–120° for CeB_3O_6). The digitization of the powder pattern was carried out with a 0.03° step. All powders were sieved at 200 μm to obtain a plane sample surface and minimize statistical orientation.

Based upon the structural arrangements of the o- [8] and m-$LaBO_3$ [9] and LaB_3O_6 [10], the cell parameters and the atomic positions of cerium derivatives phases were successfully refined with the Rietveld method using the JANA2000 crystallographic program [11] (all the standard uncertainties correspond to the calculations estimated deviations output multiplied by the Berar factor [12]) ($a = 5.8125(2)$ Å, $b = 5.07801(18)$ Å, $c = 8.1947(3)$ Å, $V = 241.876(10)$ Å^3, $Z = 4$, SG: $Pnma$, $R_p = 1.61\%$ and $R_{wp} = 2.17\%$ for o-$CeBO_3$; $a = 6.3022(7)$ Å, $b = 5.0593(6)$ Å, $c = 4.1311(4)$ Å, $\beta = 107.528(8)°$, $V = 125.60(3)$ Å^3, $Z = 2$, SG: $P2_1/c$, $R_p = 2.68\%$ and $R_{wp} = 3.56\%$ for m-$CeBO_3$, $a = 9.8993(5)$ Å, $b = 8.1234(5)$ Å, $c = 7.9321(4)$, $\beta = 40.564(4)°$, $V = 414.80(6)$ Å^3, $Z = 4$, SG: $C2/c$, $R_p = 1.82\%$ and $R_{wp} = 2.48\%$ for CeB_3O_6) [6]. Tables 1 and 2 summarize the data collection conditions and the refinement results along with the atomic positions. Fig. 1 depicts the observed and calculated patterns and the difference functions of the studied materials. Note that o-$CeBO_3$ was refined taking into account the occurrence of m-$CeBO_3$ as impurity (2.3(2)% in weight and that in CeB_3O_6 case U_{iso} values for each O atom and each B atom, respectively, were constrained to be equal).

Although the refinements were satisfactory, it is to be noted that the difference functions show a few features, and that the U_{iso} of O of CeB_3O_6 are slightly negative. Note also that O(2) of o-$CeBO_3$ and B of CeB_3O_6 have

Table 1
Crystal, X-ray data collection and refinement parameters for *o*-, *m*-$CeBO_3$ and CeB_3O_6

Chemical formula	$CeBO_3$	$CeBO_3$	CeB_3O_6
Molecular weight ($g\,mol^{-1}$)	198.93	198.93	268.55
Crystal system	Orthorhombic	Monoclinic	Monoclinic
Space group	*Pnma*	$P21/c$	$C2/c$
Color	White	Light brown	White
Cell parameters			
a	5.8125(2) Å	6.3022(7) Å	9.8993(5) Å
b	5.07801(18) Å	5.0593(6) Å	8.1234(5) Å
c	8.1947(3) Å	4.1311(4) Å	7.9321(4) Å
β		107.528(8)°	40.564(3)°
V	241.876(10) $Å^3$	125.60(3) $Å^3$	414.80(6) $Å^3$
Z	4	2	4
Halfwidth parameters[a]			
GU	0.115(18)	1.19(17)	0.36(13)
GV	0.023(10)	−0.38(12)	−0.43(14)
GW		0.05(2)	0.23(4)
LX	0.0144(3)	0.0254(8)	0.077(5)
Absorption parameter: flat plate	0.14	0.12	0.12
Impurity-weight percentage	2.3(2)		
Reliability factor	$R_p = 0.0161$	$R_p = 0.0268$	$R_p = 0.0182$
	$R_{wp} = 0.0217$	$R_{wp} = 0.0356$	$R_{wp} = 0.0248$
	$\chi^2 = 2.21$	$\chi^2 = 1.05$	$\chi^2 = 8.18$
Refined parameters	38	31	42

[a] Using the Voigt function modified by Thompson et al. [34].

Table 2
Fractional atomic coordinates, equivalent isotropic displacement parameters ($Å^2$) and standard uncertainties for *o*-, *m*-$CeBO_3$ and CeB_3O_6

Atom	X	Y	Z	U_{iso}
For *o*-$CeBO_3$				
Ce	0.2571(8)	1/4	0.5842(2)	0.0044(5)
O(1)	0.410(3)	1/4	0.074(3)	0.013(5)
O(2)	0.4103(18)	0.489(3)	0.3244(19)	0.001(3)
B	0.417(8)	1/4	0.252(7)	0.058(19)
For *m*-$CeBO_3$				
Ce	0.7755(4)	1/4	0.6209(8)	0.0049(7)
O(1)	0.376(4)	1/4	0.311(6)	0.014(4)
O(2)	0.179(3)	0.018(2)	0.845(5)	0.014(4)
B	0.215(8)	1/4	−0.001(12)	0.016(15)
For CeB_3O_6				
Ce	0	0.0509(4)	1/4	0.006(3)
O(1)	0.863(3)	0.359(2)	0.284(4)	−0.001(3)
O(2)	0.861(3)	0.431(3)	0.996(3)	−0.001(3)
O(3)	0.969(3)	0.157(2)	0.986(4)	−0.001(3)
B(1)	0	0.459(8)	1/4	0.001(8)
B(2)	0.908(6)	0.317(4)	0.074(8)	0.001(8)

low U_{iso} values. These small values are to be related to the strong diffraction and absorption power of Ce.

2.3. DSC and density measurements

To study the stability of *m*-$CeBO_3$ and *o*-$CeBO_3$, differential scanning calorimetry (DSC) analyses were carried out with a Setaram TG-DSC 111, using 79.6 and 94.6 mg of powder, respectively. The samples were heated in stainless sealed crucibles up to 820°C at 1°C/min. The densities were measured with a Micromeritics AccuPyc 1330 automatic pycnometer, with 720.9 and 826.3 mg sample, respectively, for *m*-$CeBO_3$ and *o*-$CeBO_3$.

2.4. Diffuse reflectance measurements

The UV–visible diffuse reflectance spectra were recorded, on finely ground samples, with a Perkin-Elmer Lambda 900 spectrometer with a 0.1 nm

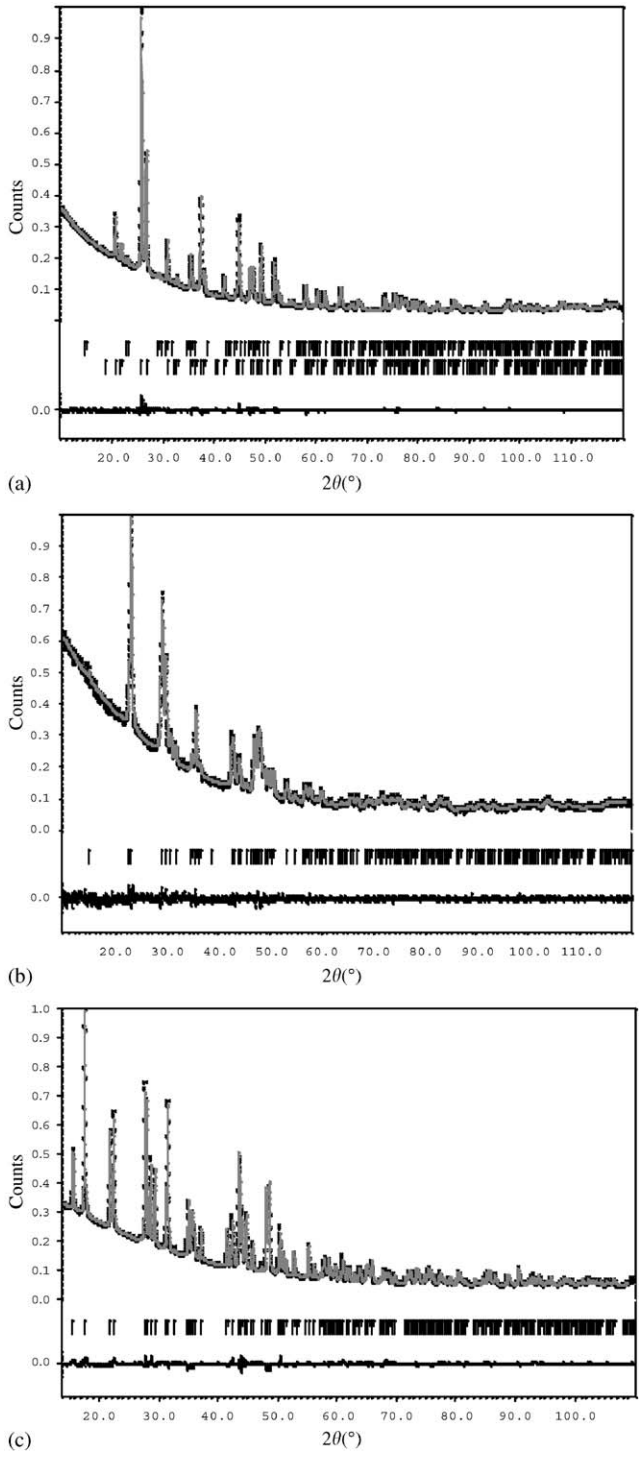

Fig. 1. Diffraction pattern, Rietveld profile and difference pattern of o-$CeBO_3$ (a), m-$CeBO_3$ (b) and CeB_3O_6 (c).

resolution. This instrument was equipped with a 150 mm diameter Labsphere integrating sphere and computer controlled using the UV Winlab software. The reflectance vs. wavelength measurements were made in the 200–700 nm range (i.e., from 2.07 to 6.20 eV) with a Spectralon® sample as reference (100% reflectance). The absorption (K/S) data were calculated from the reflectance spectra using the $K/S = (1-R)^2/2R$ Kubelka-Munk function where $R(\lambda)$, $K(\lambda)$ and $S(\lambda)$ are the reflectance, the absorption coefficient and the scattering coefficient, respectively. This formula is practically energy independent for particles larger than 5 μm [13] which is below the particle size of the samples used here. The absorption threshold was taken as the intersection point between the energy axis and the line extrapolated from the linear portion of the absorption edge in the K/S vs. E (eV) plot (Fig. 2). Due to its color heterogeneity, the optical properties of m-$CeBO_3$ were not measured. The Gaussian deconvolution of the diffuse reflectance spectra were carried out with Origin Microcal Software.

2.5. Electron energy loss spectroscopy (EELS)

EELS characterization of the powders were carried out at the RHODIA's Aubervilliers Research Center on a transmission electron microscope (TEM) Philips CM 30, LaB_6 gun, coupled with a GATAN 666 spectrometer controlled through ELP3 software. EELS experiments had two different objectives. First, boron K-edge electron loss near edge structure (ELNES) fingerprint (Fig. 3) has proven to be a very rapid and efficient way to identify the boron's environment (trigonal or tetrahedral) in the past [14]. The technique helps the structural characterization of the phases and permits the identification of phase impurities in the powder. Even when not detectable by XRD because of very low concentration, phase impurities may be found in TEM analysis. Checking the B-K ELNES fingerprint ensures that EELS optical constant measurements were performed on the correct phase. Second, EELS was used to derive the optical constant of the phases. Then, the TEM was operated at 100 kV, with an unsaturated beam, in order to optimize the spectral resolution. An FWHM of 0.8 eV is routinely achieved in these conditions. We used the image-coupling mode, where the diffraction pattern is sent in the aperture of the spectrometer. The following parameters were used: entrance aperture diameter 2 mm, energy dispersion 0.1 eV and acquisition time below 500 ms. Acquisition of spectra was made in nano probe mode on a 10–20 nm area. Electron diffraction pattern was qualitatively used to select thin area and avoid crystals which orientation corresponded to a simple crystallographic axis parallel to the electron beam. The convergence angle (3.5 mrad) was high enough to make the analysis non-orientation dependent. Eight spectra were acquired, aligned and summed together. The acquisition and comparison of spectra translated on the photodiode array made it possible to insure that the low intensity feature on the spectra in the energy range 2–5 eV are not due to a "ghost" or remnant effect after exposing the photodiode

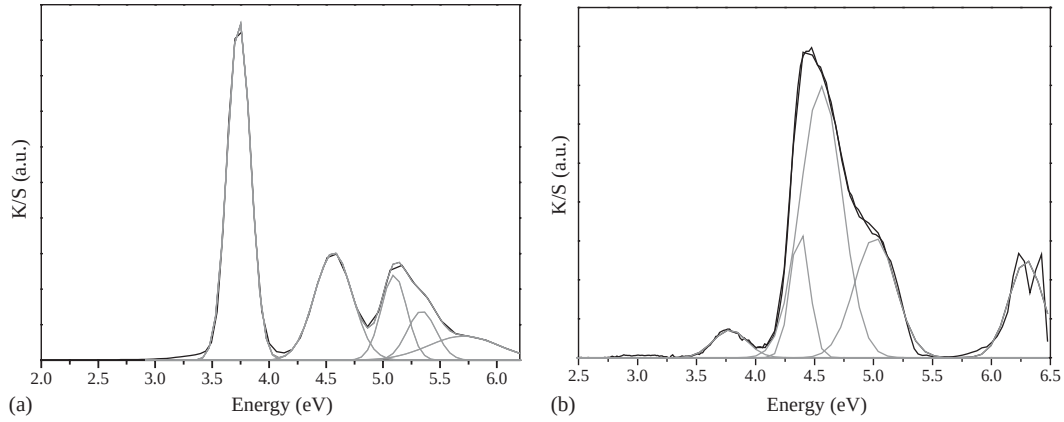

Fig. 2. Kubelka–Munk function versus energy and Gaussian deconvolution in the 2–6.2 eV range for *o*-$CeBO_3$ (a) and CeB_3O_6 (b).

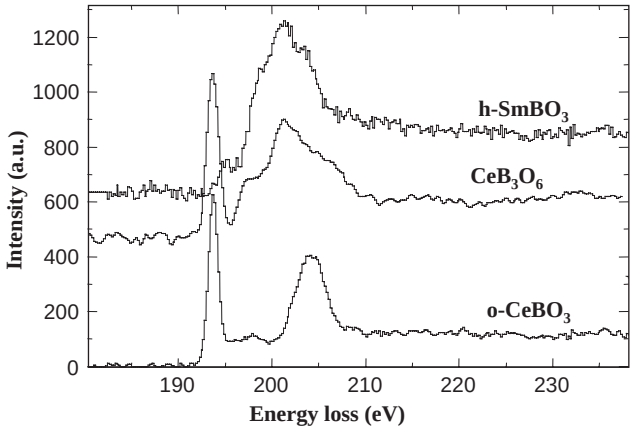

Fig. 3. Boron *K*-edge electron loss near edge structure (ELNES) for hexagonal $SmBO_3$, *o*-$CeBO_3$ and CeB_3O_6.

array with a zero loss high intensity peak, a problem that the GATAN 666 spectrometer is sensitive to.

Classically, the treatment of the spectra followed four steps: (i) extraction of data and deconvolution of multiple diffusion effects; (ii) correction for acquisition parameters (convergence and collection angles); (iii) normalization using "n_o" refractive index extrapolated to low energy (1.65 is used for borates); (iv) Kramers–Krönig analysis using the numerical integration method. The mathematics behind steps 2 and 3 have been described in detail in Egerton [15] and Montardi et al. [16]. We will insist here on the first step of the procedure which is the most important for insuring reliability of results. Most of the procedures used rely on the modeling of the zero loss peak using Gaussian and Lorenztian components and in removing this model from the raw spectrum. The experience we have with our equipment is that this method strongly underestimates the high energy part of the elastic peak, conducing in an overestimation of the intensity of the low energy part of $\mathrm{Im}(-1/\varepsilon)$. This effect, detectable below 10 eV, strongly influences the results below 5 eV. The procedure also generates artifacts in the 0–3 eV region. To overcome this problem we separated this procedure into two steps. First, we extract the relevant information from the raw spectrum using a modeling of the high energy side of the zero loss using the $A.e^{-r}$ power law imbedded in the ELP software for background subtraction. The energy window (1 eV) used for the modeling was placed below the optical gap for the product. Various data can be used for that: known gap, powder color, diffuse reflection measurements, etc. The precise position is tested for minimum artifact and the useful signal is then retrieved using the "background subtraction" function in the ELP program. Second, we computed a model of the zero loss peak using the computed thickness function in ELP: a composite spectrum was then built by adding the Zero Loss peak model with the extracted data. The behavior of this spectrum in ELP's Fourier ratio deconvolution procedure to obtain the imaginary part of the dielectric function $\mathrm{Im}(-1/\varepsilon)$ gave good results.

At the end, since the loss function is a causal response, the real part of the dielectric function can be calculated from the imaginary part with the Kramers–Krönig relation:

$$\mathrm{Re}\left(\frac{1}{\varepsilon(E)}\right) = 1 - \frac{2}{\pi} P \int_0^{\infty} \mathrm{Im}\left(\frac{-1}{\varepsilon(E)}\right) \frac{E'}{E'^2 - E^2}\, \mathrm{d}E',$$

where P is the principal part of the Cauchy integral. The complex dielectric function $\varepsilon = \varepsilon_1 + i\varepsilon_2$ and the complex refractive index $N = n + ik$ (with n the refractive index and k the extinction coefficient) were calculated, according to $\varepsilon_1 = n^2 - k^2$ and $\varepsilon_2 = 2nk$ (cf. Fig. 4).

2.6. Band structure calculations

The full-potential linearized augmented plane wave (FP-LAPW) method implemented in the WIEN2K code [17] was used for band structure calculations. In the LAPW method, the unit cell is divided into two types of

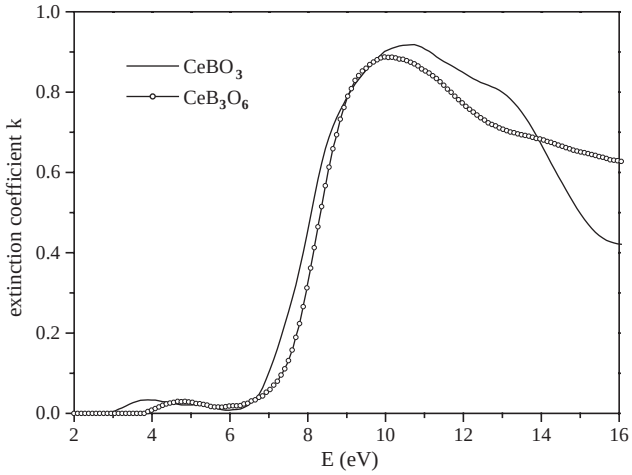

Fig. 4. Extinction coefficient versus energy in the 2–16 eV range for *o*-$CeBO_3$ and CeB_3O_6.

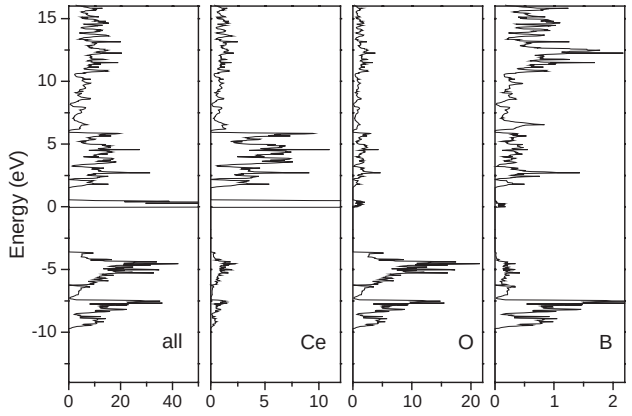

Fig. 5. Total density of state (DOS) and DOS projected along the different elements for *o*-$CeBO_3$.

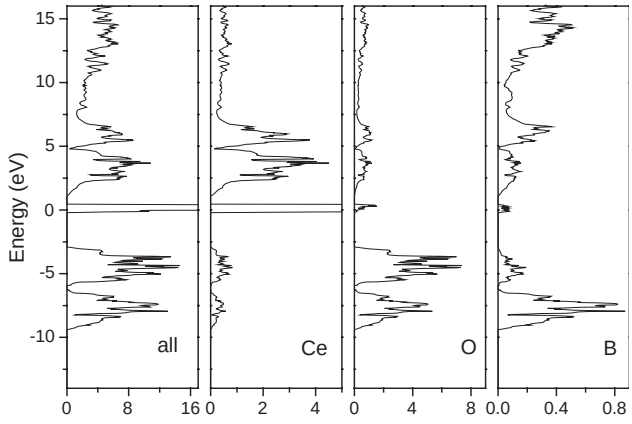

Fig. 6. Total density of state (DOS) and DOS projected along the different elements for *m*-$CeBO_3$.

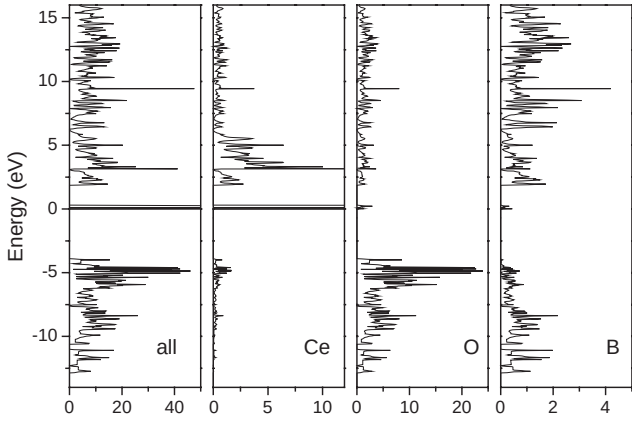

Fig. 7. Total density of state (DOS) and DOS projected along the different elements for CeB_3O_6.

regions, the atomic spheres centered upon nuclear sites and the interstitial region between the non-overlapping spheres. Inside the atomic spheres, the wave functions are replaced by atomic-like functions while in the interspheres region, the wave function of a Bloch state is expanded in plane waves. The exchange and correlation effects were treated within the density functional theory (DFT) using the Perdew–Burke–Ernzerhof generalized gradient approximation (GGA) [18]. The maximum l value in the expansion of the basis set inside the atomic sphere was 12 for the computation of muffin-tin matrix and 4 for the non-muffin-tin matrix element. The convergence of the basis set was controlled by a cutoff parameter $R_{mt} \times K_{max} = 6$ where R_{mt} is the smallest atomic sphere radius in the unit cell and K_{max} is the magnitude of the largest k vector. The self-consistency was carried out on a 12, 24 and 10 k-points in the irreducible Brillouin zone for *o*-, *m*-$CeBO_3$ and CeB_3O_6 respectively, with the following radii $R_{mt}(Ce) = 2.4$ a.u., $R_{mt}(O) = R_{mt}(B) = 1.23$ a.u. and GMAX = 14 $Bohr^{-1}$(Figs. 5–7).

The dielectric function of an anisotropic material is a complex symmetric second-order tensor which describes the linear response of an electronic system to an applied external electric field. The imaginary part of the dielectric tensor is directly related to the electronic band structure of a solid, so it can be computed from the knowledge of single-particle orbitals and energies approximated by the solutions of the Kohn–Sham equations. However, it is a well known fact that DFT calculations underestimate the band gap. To take this into account, a "scissors operator" was used, allowing a shift of the bands situated above the valence band and a rescaling of the matrix elements [19,20]. Hence, assuming the one-electron, rigid band approximation, neglecting electron polarization effects (Koopmans' approximation) and in the limit of linear optics and of the visible–ultraviolet region, the imaginary part

of a matrix element of the dielectric tensor $\varepsilon_{\alpha\beta}$ is given by [21,22]:

$$\mathrm{Im}\,\varepsilon_{\alpha\beta}(\omega) = \frac{4\pi^2 e^2}{m^2(\omega - \Delta_C/h)^2}\sum_{i,f}\int_{BZ}\frac{2\,\mathrm{d}k^3}{(2\pi^2)} \times \langle i_k|p_\beta|f_k\rangle\langle i_k|p_\alpha|i_k\rangle \times \delta(E_f(k) + \Delta_C - E_i(k) - \hbar\omega)$$

for a vertical transition from a filled initial state $|i_k\rangle$ of energy $E_i(k)$ to an empty final state $|f_k\rangle$ of energy $E_f(k)$, with wave vector k. Δ_C is the shifting value of the scissors operator, ω the frequency of the incident wave, e the electron charge, m the free electron mass and p_α is the Cartesian components of the momentum operator. As mentioned before, the real and the imaginary parts are linked by a Kramers–Krönig transformation. This is used to obtain the real part $\varepsilon_1(\omega)$, a Lorentzian broadening of 0.05 eV being used. In order to get the isotropic dielectric function, the components of the matrix trace were averaged (i.e., $\varepsilon_{iso} = 1/3(\varepsilon_{xx} + \varepsilon_{yy} + \varepsilon_{zz})$). The complex refractive index was thus calculated with the formulas given above. For dielectric tensor calculation, the BZ integration was made with 60, 108 and 54 independent k-points for o-, m-$CeBO_3$ and CeB_3O_6, respectively. Finer k-point grids did not modify the dielectric tensor values. Moreover, since localized 4f electrons are treated as delocalized one in the Wien code and as no Hubbard term (on-site electron repulsion energy) was taken into account for the dielectric tensor calculation, $f-f$ and O2p−Ce4f transition contributions, not observed experimentally, were calculated separately and subsequently subtracted from the imaginary part of the dielectric function before a Kramer–Krönig transformation (Figs. 8–10).

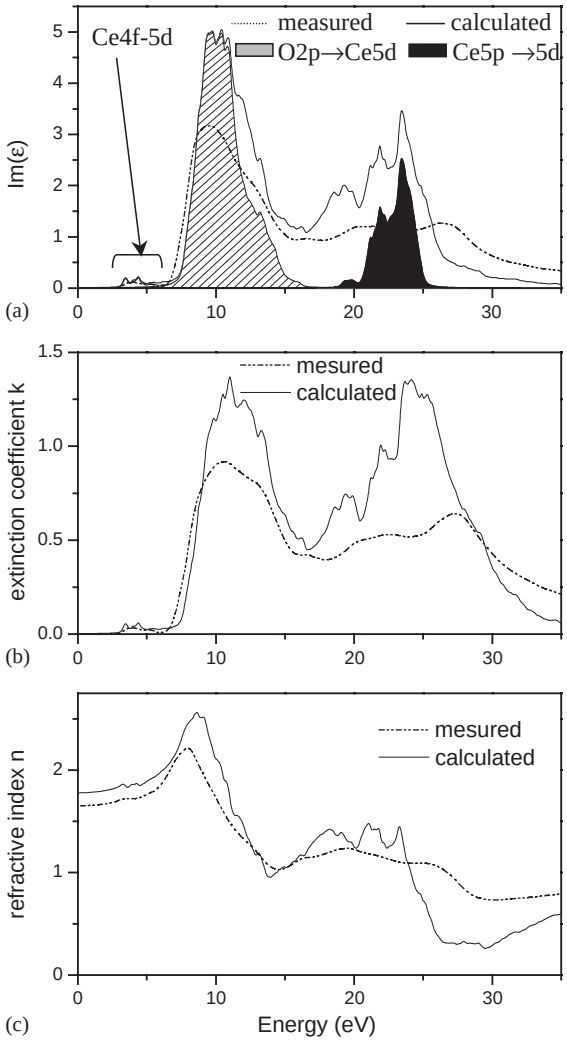

Fig. 8. Measured and calculated isotropic imaginary part of the dielectric function (a), with Ce 4f→5d, Ce 5p→5d and O2p→Ce5d transitions contributions, extinction coefficient k (b) and refractive index n (c) in the 0–35 eV range, for o-$CeBO_3$.

3. Results and discussion

3.1. Structural aspects

(a) *$CeBO_3$ allotropes*: m-$CeBO_3$ and o-$CeBO_3$ crystallize in the known H–$LaBO_3$ [23] and aragonite [8] structure types, respectively. The two varieties exhibit three-dimensional structures built upon [CeO_9] polyhedra and [BO_3] planar triangles. In m-$CeBO_3$, a cerium polyhedra is surrounded by ten [CeO_9] congeners sharing eight edges and two corners, and by six [BO_3] units sharing three edges and three corners. In o-$CeBO_3$, [CeO_9] building blocks share six corners and six edges with 12 adjacent [CeO_9] polyhedra, and three corners and three edges with six [BO_3] triangles. For the two structures, the Ce–O and B–O distances turn out to be similar (Table 3) ranging from 2.44(2) to 2.748(11) Å, and from 1.32(3) to 1.38(5) Å for m-$CeBO_3$ ($\overline{Ce-O}$ = 2.588 Å, $\overline{B-O}$ = 1.34 Å), and from 2.396(18) to 2.720(6) Å, and from 1.35(3) to 1.46(6) Å for o-$CeBO_3$ ($\overline{Ce-O}$ = 2.566 Å, $\overline{B-O}$ = 1.39 Å). These distances, almost identical to those observed in the lanthanum derivatives [8,23], agree well with the sum of the associated ionic radii $(R(Ce^{3+}_{IX})) = 1.196$ Å, $(R(B^{3+}_{III})) = 0.01$ Å, $(R(O^{2-}_{IV})) = 1.38$ Å) [24] and with the charge balance $Ce^{3+}B^{3+}O_3^{2-}$. Nevertheless, in spite of similar building entities, the difference in their structural arrangement leads to a volume per formula unit significantly different, that are 63.15(9) Å^3 and 60.469(10) Å^3 for the monoclinic and the orthorhombic forms, respectively, associated to density values of 5.26 and 5.46 (4.4% difference). These values perfectly match the measured densities, 5.16 and 5.41, respectively (4.8% difference).

The DSC curve for m-$CeBO_3$ exhibits an exothermic reaction peak at 721°C which corresponds to the transformation of the low temperature form into the high temperature form, i.e., the transition m-$CeBO_3$→

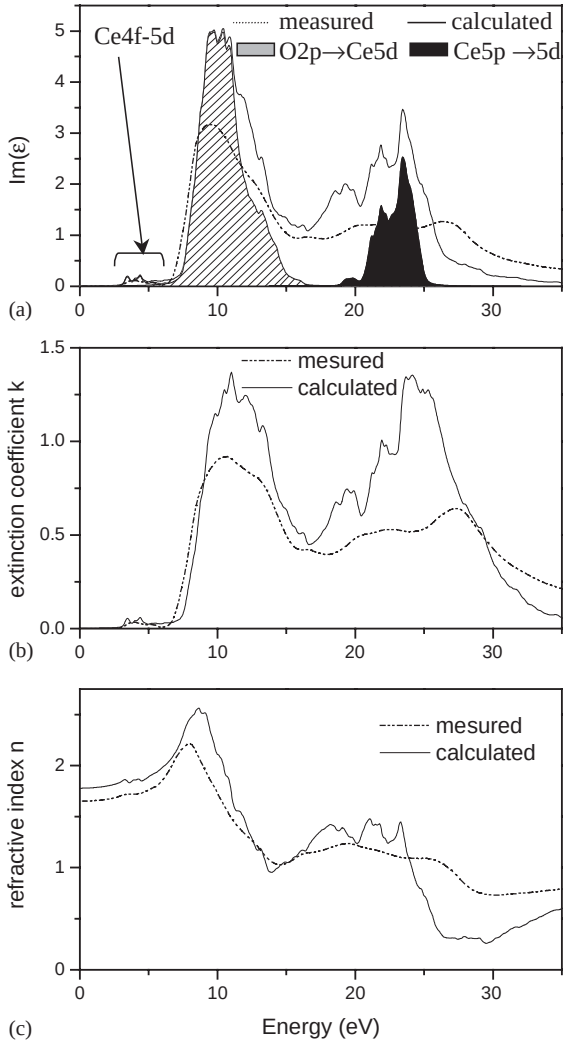

Fig. 9. Same as Fig. 8 (without measured spectrum) for m-$CeBO_3$.

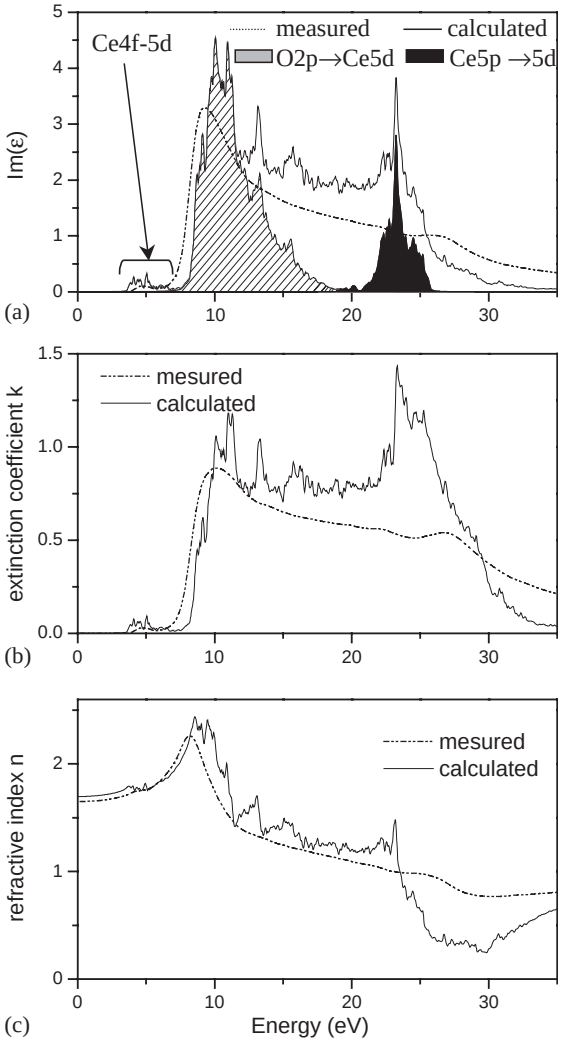

Fig. 10. Same as Fig. 8 for CeB_3O_6.

o-$CeBO_3$. In contrast, the orthorhombic form undergoes no transformation in the examined temperature range. This indicates that the orthorhombic form is the most stable one. This goes along with a volume per formula unit greater for m-$CeBO_3$ than for o-$CeBO_3$. The observed transition temperature for m-$CeBO_3$ agrees well with that reported by Lemanceau et al. [25] for m-$LaBO_3$ (720°C). However note, according to Levin et al. [26] and Böhlhoff et al. [9,23], an orthorhombic to monoclinic reverse transformation takes place, also, for $LaBO_3$ at about 1500°C. Such a transition could occur also for $CeBO_3$. So far, no explanation is given concerning the possible stabilization of the same monoclinic form at low (<720°C) and high temperatures (>1500°C) while the orthorhombic form is prepared at an intermediate temperature.

(b) *CeB_3O_6*: CeB_3O_6 is isostructural to LaB_3O_6 which structure has already been reported by Abdullaev et al. [10]. The charge balance is $Ce^{3+}B_3^{3+}O_6^{2-}$. Cerium cations are coordinated tenfold by oxygen, and each Ce polyhedron is surrounded by four edge sharing congeners to give rise to a three-dimensional $^3_\infty[CeO_6]$ network. Boron atoms, present as tetrahedrally $[BO_4]$ units (1/3) and triangular $[BO_3]$ units (2/3), are connected to $[CeO_{10}]$ polyhedra through the sharing of three edges and one edge and three corners, respectively. To some extent, CeB_3O_6 may be regarded as $^1_\infty[B_3O_6]$ chains, running along the c-axis and built upon the regular succession of $[BO_4]$ tetrahedra sharing four corners with monodentate $[BO_3]$ triangles, separated from each other by Ce cations. Ce–O distances (Table 3) range from 2.76(2) to 2.36(3) Å ($\overline{Ce-O} = 2.57$ Å) and are in agreement with the sum of the ionic radii. B(1) in tetrahedral coordination and B(2) in triangular coordination exhibit distances ranging from 1.41(5) to 1.56(4) Å ($\overline{B-O} =$ 1.48 Å), and from 1.37(7) to 1.40(8) Å ($\overline{B-O} = 1.38$ Å), respectively. This agrees well with an increase of the B^{3+} radius with the coordination, $d(B_{IV}^{3+}-O_{IV}^{2-}) = 1.49$ Å and $d(B_{III}^{3+}-O_{IV}^{2-}) = 1.39$ Å.

Table 3
Interatomic distances (Å) and, between bracket, corresponding standard uncertainties

o-$CeBO_3$		*m*-$CeBO_3$		CeB_3O_6	
CeO_9 site		CeO_9 site		CeO_{10} site	
Ce–O1	2.396(2) (× 1)	Ce–O2	2.44(2) (× 2)	Ce–O3	2.36(3) (× 2)
Ce–O2	2.459(12) (× 2)	Ce–O1	2.46(2) (× 1)	Ce–O3	2.49(4) (× 2)
Ce–O2	2.563(14) (× 2)	Ce–O2	2.532(19) (× 2)	Ce–O2	2.61(2) (× 2)
Ce–O2	2.609(14) (× 2)	Ce–O2	2.697(16) (× 2)	Ce–O1	2.631(16) (× 2)
Ce–O1	2.720(6) (× 2)	Ce–O1	2.748(11) (× 2)	Ce–O1	2.76(2) (× 2)
$\overline{Ce-O}$	*2.566(12)*	$\overline{Ce-O}$	*2.588(17)*	$\overline{Ce-O}$	*2.57(3)*
BO_3 site		BO_3 site		BO_3 site	
B–O2	1.35(3) (× 2)	B–O2	1.32(3) (× 2)	B2–O3	1.37(7) (× 1)
B–O1	1.46(6) (× 1)	B–O1	1.38(5) (× 1)	B2–O2	1.38(4) (× 1)
				B2–O1	1.40(8) (× 1)
$\overline{B-O}$	*1.39(4)*	$\overline{B-O}$	*1.34(4)*		
				$\overline{B-O}$	*1.38(6)*
				BO_4 site	
				B1–O1	1.41(5) (× 2)
				B1–O2	1.56(4) (× 2)
				$\overline{B-O}$	*1.48(4)*

Note: In italic, average distances (× 1 and × 2 indicate the number of equivalent bond distances).

3.2. Boron-K ELNES characterization

Typical Boron *K*-edge ELNES spectra of hexagonal $SmBO_3$ [27] and *o*-$CeBO_3$ are presented in Fig. 3. The major difference between the two phases lies in the boron coordination, $SmBO_3$ containing $[BO_4]$ building blocks while *o*-$CeBO_3$ contains only $[BO_3]$ triangles. In spite of the proximity of intense Sm–N4.5 or Ce–N4.5 peak, the B *K*-edge beginning at ~190 eV is easily visible. The B *K*-edge fine structure in these compounds can be compared with the reference spectra for B_2O_3 or BPO_4 [14]. BO_3 plane trigonal configuration in *o*-$CeBO_3$ is characterized by a first sharp peak at 192 eV followed by a large peak at 205 eV. This fine structure is very similar to that of the carbon *K*-edge fine structure in carbonate where C is surrounded also by 3 oxygen atoms in a plane. In contrast, tetragonal BO_4 configuration in hexagonal $SmBO_3$ is characterized by a single broad peak extending from 195 to 205 eV where different structures can be seen. For CeB_3O_6 the fine structure presents features characteristic of BO_3 and BO_4 configurations, which is in agreement with the mixed (trigonal/tetragonal) environment of boron atoms as shown by the XRD structural study. Thus ELNES appears as an appropriate technique to probe the boron environment.

3.3. Optical properties

The diffuse reflectance spectra (Kubelka–Munk transformed) of *o*-$CeBO_3$ and CeB_3O_6 (Fig. 2) can be viewed as containing five Gaussian-like absorption bands in the [3–6.5] eV range (Table 4). Due to their shape and location in energy, these bands can be assigned to $4f-5d$ electronic transitions (see below). The vb to cb charge transfer occurring at energies higher than 6.5 eV (cf. Section 1) is then not visible on these spectra.

Table 4
Ce $4f$–$5d$ diffuse reflectance peaks maxima (eV) for *o*-$CeBO_3$ and CeB_3O_6

$CeBO_3$		CeB_3O_6	
This work	Ref. [28]	This work	Ref. [28]
3.74	3.75	3.78	
4.56	4.66	4.37	4.59
5.10	5.15	4.56	4.77
5.34	5.34	5.01	5.04
5.71	5.77		5.66
		6.29	6.08

The positions in energy of the absorption bands of *o*-$CeBO_3$ agree well with those previously reported for a cerium doped lanthanum orthoborate, *o*-$LaBO_3$:Ce [28] (Table 4). This indicates that the local Ce chemical environment is the same in the $LaBO_3$ host lattice as it is in pure *o*-$CeBO_3$. This absence of the chromatic effect can be explained in terms of a crystal relaxation around Ce^{3+} as already observed for the $Y_{1-x}Ce_xPS_4$ solid solution (same ionic radius of Y^{3+} and La^{3+}, 1.06 Å, and Ce^{3+} radius of 1.22 Å) [29]. In contrast, our results for CeB_3O_6 do not match those reported by Dorenbos

et al. [28,30] and Knittel et al. [31] for LaB_3O_6:Ce^{3+}. This discrepancy may originate from a contamination of the sample by *o*-$CeBO_3$, as proposed by Knittel et al. [31].

Fig. 4 shows the observed extinction coefficient versus energy (2–16 eV range) obtained on powder from EELS for *o*-$CeBO_3$ and CeB_3O_6. Both compounds exhibit, firstly, a weak absorption band spreading from 3 to 6 eV, with an extinction coefficient maximum (k_{max}) of about 0.035 and, secondly, an intense absorption band at 6.92 and 7.36 eV, for *m*-$CeBO_3$ and CeB_3O_6 respectively, which extends up to at least 16 eV, with a k_{max} of about 0.9. As mentioned earlier, the first absorption threshold can be attributed to the symmetry and spin allowed interband, intrasite Ce^{III} 4*f*–5*d* transition, while the steep absorption onset is due to the $O^{2-}(2p)$–$Ce^{3+}(5d)$ charge transfer. As already observed in the well-studied γ-Ce_2S_3:*A* (*A* = alkali-metal) pigments series (Y. Montardi, private communication), the spin and parity allowed Ce-4*f*–5*d* transition turns out to be much less intense than the charge transfer. This could originate (i) from the small radial extent of the 4*f* wave function [32] (with a poor delocalization of *f* electrons and hence an intrasite character of the transition) compared to extended O2*p* orbitals which make the cross-section of Ce-4*f*–5*d* transition low; and (ii) from a concentration in Ce-$4f^1$ electrons much lower than that of O-2*p* electrons. Thus, the *f* to *d* electronic transition appears inappropriate in the quest of high absorbing materials.

3.4. Electronic structures

The total density of states (DOS) in the [−14; +16] eV range of *o*-$CeBO_3$, *m*-$CeBO_3$ and CeB_3O_6 are displayed in Figs. 5–7 with the atomic site-projected contributions. The zero energy is taken at the Fermi level. In all materials, the DOS curve can be subdivided into three regions.

Below –3 eV is found the valence band (vb) built upon oxygen 2*p* orbitals. In *o*-$CeBO_3$ and *m*-$CeBO_3$, an analysis of the DOS evidences that this band can be split in two parts. The bottom is built upon O-orbitals strongly hybridized (then stabilized) with B-ones (strong covalent character of the B–O bonds within the isolated BO_3 triangles), while the top consists in O-orbitals mainly engaged in less stabilizing Ce–O orbital interactions (ionic character of the Ce–O bond). These features are less evident for CeB_3O_6 because of the multiple oxygen environments and because of the occurrence of infinite $\frac{1}{\infty}[B_3O_6]$ chains which give rise to more dispersed electronic states than those observed in isolated $[BO_3]$ entities. Moreover, for both $CeBO_3$ forms, all oxygen atoms are surrounded by three cerium atoms and one boron atom, whereas in CeB_3O_6, for O1, O2 and O3, the number of linked cerium and boron are 2/2, 1/2 and 2/1, respectively. Consequently, the O3′ projected DOS is more important at the top of the O2*p* band than that of O1 and O2, whereas the inverse is observed at the bottom of the vb. Another consequence of the diversity in the O environments and in the dimensionality of the B/O network is the increase of the O2*p* bandwidth, 6.1 and 6.3 eV, for *o*-$CeBO_3$ and *m*-$CeBO_3$ respectively, versus 9 eV for CeB_3O_6.

Beyond 1 eV is located the conduction band (cb) which bottom consists mainly of Ce-5*d* orbitals (at least up to 6–7 eV). The boron contribution (2*s* and 2*p* orbitals) to the cb appears much more diluted in energy than that of Ce-5*d* and almost negligible at the bottom. The calculated widths of the Ce5*d* bands are very similar for *o*-$CeBO_3$ and CeB_3O_6, i.e., about 4.4 eV. In contrast *m*-$CeBO_3$ exhibits a Ce5d band of 6.4 eV width with a marked splitting in two blocks. Up to now, this phenomenon remains unexplained.

Going from *o*-$CeBO_3$ to CeB_3O_6, both EELS measurement and DFT calculation show a widening of the O2*p*–Ce5*d* gap of about 0.5 eV (6.92 and 7.36 eV for EELS, 5.16 and 5.73 eV for DFT, respectively). Two effects can be involved to explain such an evolution: a more important destabilization of the Ce5*d* orbitals with increasing Ce coordination [33] (9 and 10 for *o*-$CeBO_3$ and CeB_3O_6, respectively) and a more important stabilization of the O2*p* by covalent bonding with an increasing B/O ratio.

Between the vb and cb localized 4*f* levels are interspaced, one fourteenth being occupied. Recall that the requested energy to add an extra electron on the Ce^{3+}-4*f* orbitals is estimated at about 6 eV due to the low spatial extension of the *f* orbitals and the onsite electron repulsion energy. As a consequence, the first electronic transitions, observed experimentally around 3.5 eV by diffuse reflectance (Fig. 2), can only originate from a Ce^{3+}-$4f^1 \rightarrow 5d^0$ transition. The high intensity of the absorption at about 7 eV (Fig. 4) rules out inter cerium $4f^1 + 4f^1 \rightarrow 4f^2 + 4f^0$ transitions (expected to be very weak) and its position in energy excludes also the O2*p* → Ce4*f* transition. Consequently, this absorption may only be assigned to the vb–cb charge transfer.

3.5. Dielectric constant calculation

Based on the results of our electronic structure calculations, the imaginary part $\varepsilon_2(E)$ of the dielectric function has been calculated up to 40 eV. As described in the experimental section, the conduction band positions have been corrected by a "scissors operator" of 1.65, 1.75 and 1.8 eV for *o*-$CeBO_3$, *m*-$CeBO_3$ and CeB_3O_6, respectively, to fit the observed bv–bc gap determined by EELS. In Figs. 8–10a are plotted the experimental (when measured by EELS) and the calculated isotropic imaginary part of the complex dielectric function in the [0–35] eV range for *m*-$CeBO_3$,

o-$CeBO_3$ and CeB_3O_6, respectively, with the Ce $4f \rightarrow 5d$, Ce $5p \rightarrow 5d$ and O$2p \rightarrow$Ce$5d$ transitions contributions. It can be noticed that the calculated curves reveal structures similar to the experimental ones, namely a weak peak at about 5 eV associated to the Ce $4f \rightarrow 5d$ absorption and two wide peaks centered around 12 and 25 eV respectively, corresponding to the O$2p \rightarrow$Ce$5d$ and Ce $5p \rightarrow 5d$ transition, respectively. The remaining intensity can be explained by transitions occurring from the Ce$5p$ and O$2p$ bands towards energy levels of the cb with B$2p$ character. It should be noted that the difference in the third peak position between experimental and theoretical curves can be explained by the fact that DFT allows to calculate only the fundamental state, so that the higher the energy, the lower the reliability. Thus, calculations reproduce the experimental behavior rather well.

The extinction coefficient k and the refractive index n, obtained by the method given in the experimental part, are shown on Figs. 8–10 b and c. Again, our theoretical calculations are comparable to the experimental data, the shape of the calculated curve exhibiting the same features as the experimental ones, as for $\varepsilon_2(E)$. It is worth noticing that the calculated refractive index of about 1.7 in the visible range corresponds to the expected values.

4. Conclusion

In the framework of the research of second generation UV absorbers, cerium (III) borates o-$CeBO_3$, m-$CeBO_3$ and CeB_3O_6, all isostructural of the lanthanum phases, were synthesized, and structurally and optically characterized. The Ce$4f$–$5d$ transition threshold for o-$CeBO_3$ and CeB_3O_6 are 3.45 and 3.5 eV, that is to say 0.5 eV above the required 3 eV for a UV shield. This high threshold could possibly be modified by suitable substitutions. However, the intensity of this transition, as compared to the O$2p$–Ce$5d$ charge transfer, shows that the latter is ten times more intense than the former, although both are allowed (low absorption cross-section and weak concentration in $4f$ electron case could explain this discrepancy). Due to this important drawback, and although the refractive indexes of the cerium borates are in the desired range, it is clear that the use of the Ce$4f$–$5d$ transition for UV absorption in this family of compounds cannot be contemplated. Moreover, the perfect fitting of the measured and calculated imaginary part of the dielectric function, the extinction coefficient and the refractive index evidence the ability of band structure calculation to predict reliably the optical properties of inorganic materials. Consequently, such calculations appear appropriate in the coming step to better understand the chemical factors which govern the n and k parameters, which are important with regard to the application field under study.

Acknowledgment

The research has been made possible by a Grant (No. N2/007070) from Rhodia Electronics and Catalysis.

References

[1] K.C. Mishra, B.G. DeBoer, P.C. Schmidt, I. Osterloh, M. Stephan, V. Eyert, K.H. Johnson, B. Bunsenges, Phys. Chem. 102 (1998) 1772.
[2] J. Li, C.G. Duan, Z.Q. Gu, D.S. Wang, Phys. Rev. B 57 (1998) 6925.
[3] H. Yoshida, Displ. Devices 16 (1998) 32.
[4] C.H. Kim, I.E. Kwon, C.H. Park, Y.J. Hwang, H.S. Bae, B.Y. Yu, C.H. Pyun, G.Y. Hong, J. Alloys Compd. 311 (2000) 33.
[5] S. Scalia, J. Chromatogr. A 870 (2000) 199.
[6] G. Gesenhues, Polym. Degrd. Stab. 68 (2000) 185.
[7] R.R. Reddy, A. Nazeer Ahammed, K. Rama Gopa, D.V. Raghuram, Opt. Mater. 10 (1995) 95.
[8] G.K. Abdullaev, G.G. Dzhafarov, K.S. Mamedov, Azerb. Khim. Zh. 1976 (1976) 117.
[9] R. Böhlhoff, H.U. Bambauer, W. Hoffmann, Naturwissenschaften 57 (1970) 129.
[10] G.K. Abdullaev, K.S. Mamedov, G.G. Dzhafarov, Naturwissenschaften 57 (1970) 129.
[11] V. Petricek, M. Dusek, The crystallographic computing system JANA2000. Institute of Physics, Praha, Czech Republic, 2000.
[12] J.F. Bérar, P. Lelann, J. Appl. Cryst. 24 (1991) 1.
[13] G. Kortüm, Reflectance Spectroscopy, Springer, Berlin, 1969.
[14] R. Brydson, H. Sauer, W. Engel, E. Zeitler, Microsc. Microanal. Microstruct. 2 (1991) 159.
[15] R.F. Egerton, Electron Energy Loss Spectroscopy in the Electron Microscope, Plenum Press, New York, 1986.
[16] Y. Montardi, C. Witz, L. Normand, A. Thorel, J. Phys. IV 9 (1999) 217.
[17] P. Blaha, K. Schwartz, G.K.H. Madsen, D. Kvasnicka, J. Luiz, In WIEN2K An Augmented Plane Wave + Local Orbitals Program for Calculating Crystal Properties, Techn. Universität Wien, Austria, 2001.
[18] J.P. Perdew, S. Burke, M. Erzenrhof, Phys. Rev. Lett. 77 (1996) 3865.
[19] P. Puschnig, C. Ambrosch-Draxl, Phys. Rev. B 60 (1999) 7891.
[20] R. Del Sole, R. Girlanda, Phys. Rev. B 48 (1993) 11789.
[21] F. Bassani, G. Pastori Parravicini, R.A. Ballinger, Electronic States and Optical Transitions in Solids, Pergamon Press, Oxford, 1975.
[22] W.D. Lynch, in: E.D. Palik (Ed.), Handbook of Opticals Constants of Solids, Academic Press, New York, 1985, p. 189.
[23] R. Böhlhoff, H.U. Bambauer, W. Hoffmann, Z. Kristallogr. 133 (1971) 386.
[24] R.D. Shannon, Acta Cryst. A 32 (1976) 751.
[25] S. Lemanceau, G. Bertrand-Chadeyron, R. Mahiou, M. El-Ghozzi, J.C. Cousseins, P. Conflant, R.N. Vannier, J. Solid State Chem. 148 (1999) 229.
[26] E.M. Levin, R.S. Roth, J.B. Martin, Am. Mineral. 46 (1961) 1030.
[27] G. Chadeyron, M. El-Ghozzi, R. Mahiou, A. Arbus, J.C. Cousseins, J. Solid State Chem. 128 (1997) 261.
[28] D. Dorenbos, Phys. Rev. B 64 (2001) 125117.

[29] G. Gauthier, Y. Klur, A. Pourpoint, S. Jobic, G. Ouvrard, R. Brec, D. Huguenin, P. Macaudière, Int. J. Inorg. Mater. 2 (2000) 717.
[30] D. Dorenbos, J. Lumin. 91 (2000) 155.
[31] M.J. Knitel, D. Dorenbos, C.W.E. van Eijk, B. Plasteig, B. Viana, A. Kahn-Harari, D. Vivien, Nucl. Instrum. Methods A 443 (2000) 364.
[32] K.J. Kim, B.N. Harmon, W.D. Lynch, D.D. Koelling, Phys. Rev. B 44 (1991) 8526.
[33] G. Gauthier, S. Jobic, M. Evain, H.-J. Koo, M.-H. Whangbo, C. Fouassier, R. Brec, Chem. Mater. 15 (2003) 828.
[34] P. Thompson, D.E. Cox, J.B. Hastings, J. Appl. Cryst. 20 (1987) 79.